applied sciences

MDPI

*Article*

# Ti6Al4V-ELI Alloy Manufactured via Laser Powder-Bed Fusion and Heat-Treated below and above the β-Transus: Effects of Sample Thickness and Sandblasting Post-Process

**Emanuela Cerri [1], Emanuele Ghio [1,*] and Giovanni Bolelli [2]**

[1] Department of Engineering and Architecture, University of Parma, 43123 Parma, Italy; emanuela.cerri@unipr.it
[2] Department of Engineering "Enzo Ferrari", University of Modena e Reggio Emilia, 41125 Modena, Italy; giovanni.bolelli@unimore.it
* Correspondence: emanuele.ghio@unipr.it

**Abstract:** Ti6Al4V-ELI is the most-used lightweight alloy in the aerospace industrial sector thanks to its high mechanical strength and corrosion resistance. The present paper aims, firstly, to evaluate the effects induced by different heat treatments, which were performed above and below the β-transus temperature on Ti6Al4V-ELI samples manufactured via Laser Powder-Bed Fusion in different orientations (XZ, XY, Z and 45°). The first set of tensile samples and bars were heat-treated at 1050 °C × 1 h, while the second and third set were heat-treated at 704 °C × 120′ following the AMS2801 standard specification, and at 740 °C × 130′. These heat treatments were chosen to improve the as-built mechanical properties according to the ASTM F3001 and also ASTM F2924-14 standard specifications. Optical and SEM measurements reveal primary, secondary and tertiary α-laths below the β-transus, while above this temperature, the microstructure varies in relation to the sample's thickness. Secondly, this work analyzed the results obtained after a sandblasting process, which was performed on half of all the available heat-treated tensile samples, through XRD and Vickers microhardness measurements. XRD analysis also highlighted the presence of $\alpha_2$-$Ti_3Al$ and $TiAl_3$ precipitates and the microstructural change in terms of the α-phase.

**Keywords:** Ti6Al4V-ELI; α-colonies; Widmanstätten microstructure; sample thickness; Laser Powder-Bed Fusion; mechanical properties optimization; heat treatments; sandblasting process; α-case



**Citation:** Cerri, E.; Ghio, E.; Bolelli, G. Ti6Al4V-ELI Alloy Manufactured via Laser Powder-Bed Fusion and Heat-Treated below and above the β-Transus: Effects of Sample Thickness and Sandblasting Post-Process. *Appl. Sci.* **2022**, *12*, 5359. https://doi.org/10.3390/app12115359

Academic Editors: Flaviana Calignano, Diego Manfredi and Giuseppe Addamo

Received: 30 April 2022
Accepted: 24 May 2022
Published: 25 May 2022



## 1. Introduction

Metallic materials for aerospace applications must be characterized by high mechanical strength, toughness and corrosion resistance at high and low temperatures [1–4]. Commercially, pure titanium and its alloys are widely used in this application field; 155,000 kg of these materials were used in 2020 alone [5]) as inter-tank structures (also in the cryogenic stage of launch vehicles), cockpit window frames, wing boxes, fasteners, turbo engine parts, and for the aircraft fuselage, thanks to their low density (~−60% of steel) [2,6,7]. In addition to the light-in-weight requirement, Singh et al. [3] add good durability (generally 4k–8k h and 30k–60k h for military and commercial airlines, respectively), low costs (initial cost for purchasing and maintenance) and good fabricability as desirable features for aeronautical parts. Additive Manufacturing (AM) technologies meet these latter requirements in addition to reducing the design and manufacturing time with respect to the conventional manufacturing processes [1,8]. Moreover, considering the "buy-to-fly" ratio, which is the ratio between the weight of the raw material used to manufacture the mechanical component and the weight of the final component, it reaches 10:1 ÷ 20:1 for wrought-based conventional manufacturing. In opposition, "buy-to-fly" of AM of metals approaches a ratio of 1:1 due to its high material utilization in AM, the short production cycle and minimal use of tool machines [9–11]. As a matter of fact, AM technologies allow

researchers to obtain a 3D physical object through the successive addition of material (layer-by-layer) following a CAD (Computer-Aided Design) project, which is converted into an .stl file before the manufacturing process [12,13]. Despite these advantages, Froes et al. [1] affirmed that only 8.2% of the aerospace industry has adopted rapid-prototyping technology, while Gibbons et al. [14] underlined that the certification and qualification of the Laser Powder-Bed Fusion (L-PBF) process, which is an AM technology, do not differ from the conventional manufacturing process in the aerospace field.

L-PBF is a technology wherein a laser source scans and melts a powder bed that is deposited by a roller or recoater on the build platform [12]. To obtain a fully dense and high-quality sample, the following full melting criterion proposed by Tang et al. [15] must be satisfied:

$$\left(\frac{h}{W}\right)^2 + \left(\frac{t}{D}\right)^2 < 1, \quad (1)$$

where $h$ (μm) and $t$ (μm) are the hatch spacing and the layer thickness, respectively, while $W$ (μm) and $D$ (μm) are the width and the depth of the molten pool, respectively. In other words, the main process parameters that characterize the L-PBF process (laser power $P$ (W), scanning speed $v$ (mm/s), hatch spacing $h$ (mm) and the layer thickness $t$ (mm)), and influence the molten pool dimensions, need to be optimized [16–18].

Ti6Al4V-ELI (Extra-Low Interstitial) is an α + β alloy at room temperature that contains Al and V elements as α- and β-stabilizers, respectively. In addition, the O, N and C atoms (in a small amount) stabilize the hcp (hexagonal closed packed) α-phase, while Fe stabilizes the bcc (body-centered cubic) β-phase [12,19,20]. Due to the high cooling rate (up to $10^8$ K/s, [12]) that characterizes the L-PBF technology, the as-built microstructure of the Ti6Al4V-ELI sample is totally or partially formed by α′-martensite contained within columnar β-grains arranged parallel to the build direction [21,22]. Generally, the UTS (Ultimate Tensile Strength) and YS (Yield Strength) values of as-built Ti6Al4V-ELI samples reach values higher 1.1 and 1.0 GPa, respectively, which decrease when the temperature of the pre-heated build platform or the percentage of decomposed α′-martensite are increased [12,23–25]. As a matter of fact, there is $\alpha' \rightarrow \alpha$ decomposition and a subsequent loss in mechanical properties of the as-built sample if the build platform is kept at high temperature (T > 400 °C, the temperature at which the martensite decomposes [26–28]) and/or due to the different values of energy density used $\left(E = P/vht,\ \left(\mathrm{J/mm^3}\right)\right)$. At the same time, the ductility is often lower than 9% and, consequently, the minimum tensile properties required by the F3001-14 standard specification are not satisfied [20]. In this scenario, optimized heat treatments can be necessary to obtain an improved balance in mechanical properties. Due to the chemical composition of the Ti6Al4V-ELI alloy and the phase transformations that can take place during different cooling pathways, its mechanical properties can be improved and/or tailored through different heat treatments performed below or above the β-transus temperature [12,29–31]. In particular, the as-built UTS and YS always decrease for each heat treatment performed on the as-built samples [12]. As a matter of fact, also considering a fully martensitic microstructure obtained in solution heat-treated and water-quenched samples, the UTS and YS are lower than 1.0 GPa and 950 MPa, respectively, due to the presence of recrystallized equiaxed β-grains [32–34]. At the same time, the elongation values do not show continuous growth with increasing heat-treating temperatures and time due to the following reasons: firstly, the presence of columnar β-grains, which significantly influence the fracture mechanisms, remains even after the heat treatments performed below the β-transus; secondly, defects generated during the L-PBF process play a fundamental role in the premature failure of samples [12,35]. On the other hand, the best balance between tensile strength and good elongation values (16 ÷ 18%, [12]) was obtained through the bimodal microstructure achieved after cyclic annealing heat treatments [21,36].

As previously discussed, the Ti6Al4V-ELI alloy is characterized by lower contents of oxygen (max 0.13%), nitrogen, carbon and iron than the similar Ti6Al4V alloy. This difference in chemical composition confers improved values of ductility and fracture toughness,

which are required in the aerospace sector. At the same time, the surface finishing of the Ti6Al4V-ELI sample is often correlated with air/gas flow problems correlated with the aerospace applications, but there are other reasons why aerospace engineering components require suitably low roughness. In fact, this is correlated with improved corrosion and wear resistance and with reduced friction during sliding contacts; moreover, it allows the uniform coverage of a component with a thin-film coating [37–39]. Surface roughness also has a huge impact on the fatigue life of a component, which is another important factor within the space and aerospace fields [40,41]. Möller et al. [42] correlated the surface roughness with fracture toughness, but no research concerning the effects on mechanical properties of Ti6Al4V-ELI samples was found in the literature.

The present paper aims to evaluate the microstructural effects induced by different heat treatments and the resulting mechanical properties, which are compared to the current standard specifications. Firstly, it analyzes the effects of two heat treatments performed below the β-transus temperature at 704 and 740 °C following the aeronautical standard specification (AMS 2801B); secondly, it analyzes the effects of the solution heat treatment at 1050 °C, which will be the starting point of future aging heat treatments. In addition, the present work studies the impact of the different heat treatments on samples characterized by different thicknesses. As a matter of fact, distinct aerospace components can possess widely different thicknesses, which can have an effect on their microstructures. Finally, the effects induced by the sandblasting process on the heat-treated samples are evaluated in terms of mechanical properties and surface characteristics.

## 2. Materials and Methods

Ti6Al4V-ELI powder (Tekna, Sherbrooke, QC, Canada) was used to manufacture tensile samples and bars via Laser Powder-Bed Fusion technology. The powder used was characterized by a granulometry between 20 and 60 µm and by an apparent density higher than 2.2 g/cm$^3$. Its chemical composition is reported in Table 1.

**Table 1.** Nominal chemical composition of Ti6Al4V-ELI in wt.%.

| Elements | Ti | Al | V | C | Fe | O | N | H | Y |
|---|---|---|---|---|---|---|---|---|---|
| wt.% | Bal. | 6.47 | 4.06 | 0.01 | 0.21 | 0.09 | 0.01 | 0.001 | <0.001 |

Figure 1a shows a representative batch formed by 24 tensile samples and four bars directed along different directions, i.e., $0°_{XZ}$ (blue), $0°_{XY}$ (red), 45° (green) and $90°_{Z}$ (yellow), considering their major axis of symmetry. For a better understanding of the results, the tensile samples and bars were designated as reported in Table 2, where their dimensions are also listed. Three batches (Figure 1a) were manufactured through the SLM®280 (SLM solutions, Lübeck, Germany) machine following the skin-core scan strategy reported in Figure 1b, wherein the red dotted arrows indicate the laser directions. The laser scan tracks were parallel to each other and inclined by 56.5° with respect to the base of the external frame. Each layer (n) was rotated by 67° with respect to the previously solidified layer (n − 1). To manufacture all tensile samples and bars, the following process parameters were used: scanning speed of 1250 mm/s, laser power of 340 W, hatch spacing of 120 µm and layer thickness of 60 µm. The build platform was heated at 80 °C.

All batches were heat-treated at three different temperatures below (704 and 740 °C) and above (1050 °C) the β-transus following the time–temperature curves reported in Figure 2. All treatments were performed in a vacuum furnace where the samples were cooled in argon gas for 1 h. The first batch was heat-treated at 704 °C for 2 h (704 °C/120′) following the ASM2801 standard specification, the second at 740 °C for 130′ (740 °C/130′) and the third at 1050 °C for 60′ (1050 °C/60′). The latter two heat treatments were performed to obtain a possible balance between strength and ductility to satisfy the ASTM F3001 standard specification. Focusing on the 740 °C/130′, the cooling pathway (red curve) was

formed by the first step down to 520 °C in 90′ and the second down to room temperature in argon gas.

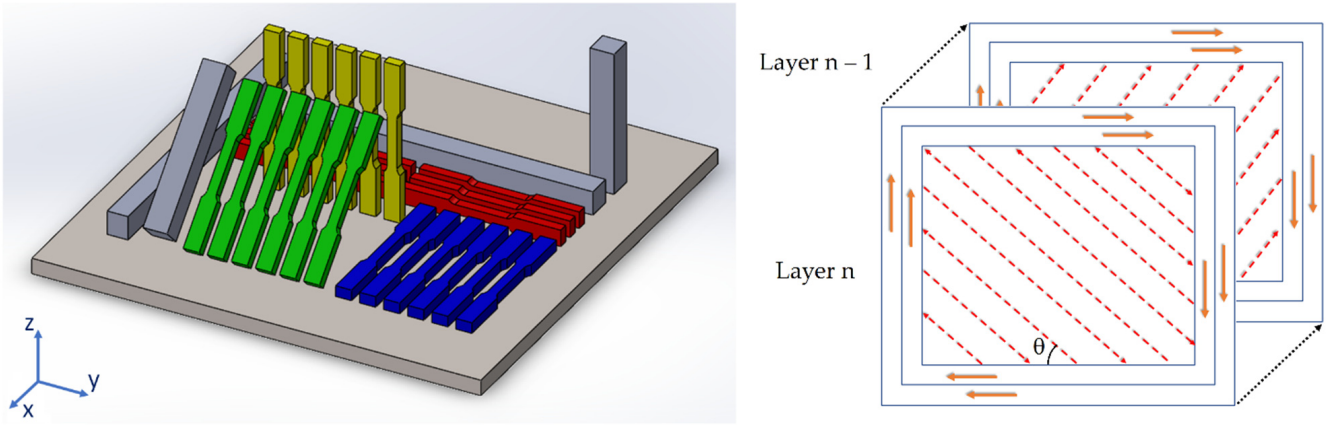


(**a**) (**b**)

**Figure 1.** (**a**) Solidworks (Dassault Systèmes, Waltham, Québec, Canada) drawing of tensile samples manufactured along the $0°_{XZ}$ (blue), $0°_{XY}$ (red), 45° (green) and $90°_{Z}$ (yellow) directions and of bars grown along the same directions; (**b**) skin-core scan strategy where θ is 56.5° and the orange and red arrows indicate the laser scans directions.

**Table 2.** Nomenclature used in the present paper for all tensile samples and bars and their dimensions.

| Samples | Nomenclature | Color | Length (mm) | Width (mm) | Thickness (mm) | Cross-Section Area ($mm^2$) |
|---|---|---|---|---|---|---|
| Tensile sample | $0°_{XZ}$-sample<br>$0°_{XY}$-sample<br>45°-sample<br>$90°_{Z}$-sample | Blue<br>Red<br>Green<br>Yellow | 10.0 [1] | 6.0 ± 0.1 [1] | 6.0 [1] | 36 |
| Bars | $0°_{XZ}$-bar<br>$0°_{XY}$-bar<br>45°-bar<br>$90°_{Z}$-bar | Grey | 25<br>10 | 15 | 15 | 225 |

[1] Dimensions in agreement with the E8/E8M-16a standard specification.

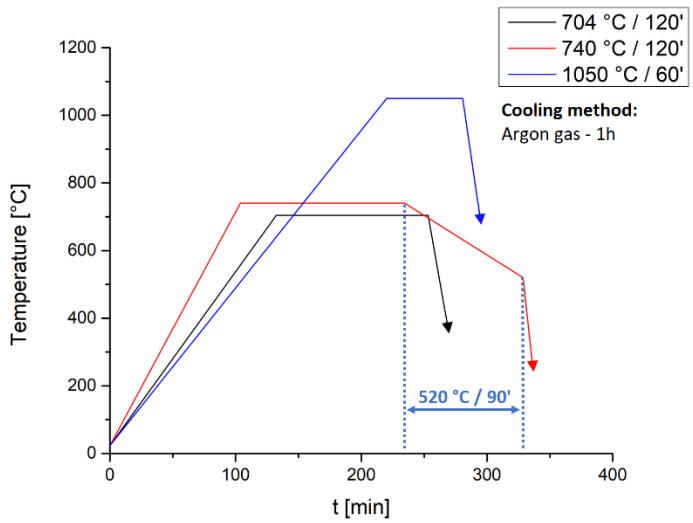


**Figure 2.** Temperature–time curves related to the heat treatment (704 °C/120′, 740 °C/130′ and 1050 °C/60′) studied in the present work.

After the heat treatments, a set of samples for each batch (Figure 1a) was sandblasted (SB) through a glass micro-sphere characterized by diameters between 200 and 300 µm. The process was performed manually with a distance of 300 mm from the sample surface and a pressure of 7 MPa. For a better understanding, all sandblasted samples will be called SB, while those characterized by an "as fabricated" surface will be called no-SB. Before and after the sandblasting process, the surface roughness was measured through an optical 3D profilometer (Taylor Hobson, Leicester, UK).

To evaluate the mechanical properties of the both SB and no-SB samples after the different heat treatments, the tensile tests were performed at room temperature with a Zwick/Roell Z100 (ZwickRoell, Einsingen, Germany) machine using a strain rate of 0.0167 $s^{-1}$. Three tensile samples were tested for each direction in SB and no-SB conditions, respectively.

Vickers microhardness measurements were performed using both 500 gf ($HV_{0.5}$) and 100 gf ($HV_{0.1}$) loads and a 15 s indentation time according to the UNI EN ISO 6507-1:2018 standard specification. In the first case, 500 gf was used to evaluate the Vickers microhardness of all samples and bars. Each $HV_{0.5}$ value was obtained as an average of nine measurements arranged within a 3 × 3 matrix where indentations were spaced 1 mm from one another (Figure 3a). On the other hand, 100 gf of load was used to evaluate the microhardness of the α-colonies, α-laths arranged in a basketweave structure, and $\alpha_{GB}$ (Grain Boundary). Finally, three microhardness profiles (Figure 3b) were performed along on the cross-sections of the $90°_Z$-samples heat-treated at 704, 740 and 1050 °C to analyze the effects induced by the sandblasting process on the surface of the SB samples. Each profile was formed by 15 indentations that were 500 µm apart, except for the 2nd from the 1st and 3rd and the 14th from the 13th and 15th, which were spaced 250 µm apart. These chosen distances satisfy the following relationship: $\delta > 2d_m$, where $\delta$ and $d$ are the distance between two successive indentations and the average value of the indentation's diagonal, respectively.

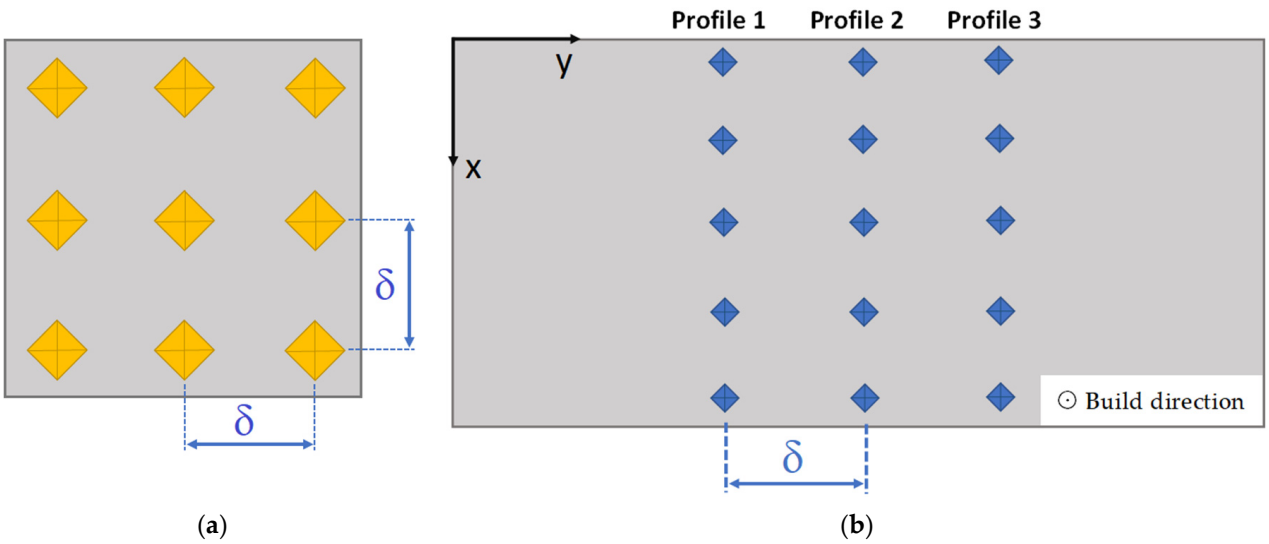


**Figure 3.** (**a**) Matrix of 3 × 3 indentations where d is 1 mm of space between two adjacent indentations; (**b**) Vickers microhardness profiles performed on cross-section of the heat-treated $90°_Z$-samples after and before the sandblasting process. Each profile is separated by $\delta$.

The heat-treated microstructures and the effects induced by the sandblasting process on the sample surface were analyzed through the DMi8 Leica optical microscope (Leica, Wetzlar, Germany) and the SEM Nova NanoSEM 450-FEI (ThermoFisher, Hillsboro, OR, USA) in parallel (xy plane, "⊙ Build direction") and perpendicular (xz plane, "↑ Build direction") directions to the build platform for $0°_{XZ}$-, $0°_{XY}$-, 45°- and $90°_Z$-samples. The thickness of α-laths and columnar β-grains was measured as reported by Gallaraga et al. [43] and

Tiley et al. [44], respectively. In addition, energy-dispersive X-ray (EDX) spectroscopy (Quantax-200, Bruker Nano GmbH, Berlin, Germany) was used to evaluate both the $\alpha'/\alpha$ and β phases and the effects induced by the sandblasting process on the sample surface.

## 3. Results

### *3.1. Microstructure and Surface Roughness*

Figure 4 shows two OM micrographs illustrating the microstructure of as-built Ti6Al4V-ELI 45°-samples on the perpendicular (Figure 4a) and the parallel (Figure 4b) planes to the build platform. Figure 4a illustrates the presence of different columnar β-grains with the white dotted lines marking their boundaries. Prior columnar β-grains are usually disposed perpendicularly to the molten pool, marked through the yellow dotted line, and totally formed by $\alpha'$-martensite laths. Figure 4b shows the cross-sections of the columnar β-grains, characterized by a typical rectangular shape. In addition, they are generally contained within the laser scan tracks (marked with dotted yellow lines). Similar results are obtained on the same types of planes of the $0°_{XZ}$-, $0°_{XY}$- and $90°_{Z}$-samples, respectively.

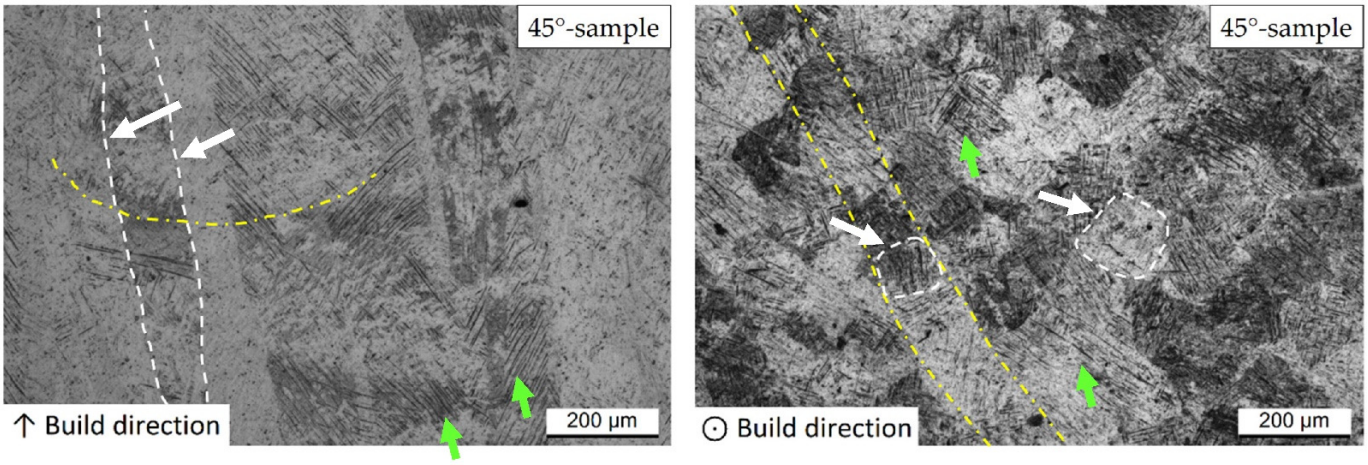


(**a**) (**b**)

**Figure 4.** OM micrographs of the microstructure of as-built Ti6Al4V-ELI 45°-sample observed: (**a**) on the plane perpendicular to the build platform, and (**b**) and on the plane parallel to the build platform. White and green arrows indicate the boundaries of the columnar β-grains (white dotted lines) and the laths of $\alpha'$-martensite, respectively. The yellow dotted lines represent the molten pool boundary (**a**), and the laser scan tracks (**b**).

Figure 5 shows the microstructure of both the $0°_{XZ}$-sample heat-treated at 704 °C/120′ (Figure 5a,b) and the $90°_{Z}$-sample treated at 740 °C/130′ (Figure 5c,d) where the columnar β-grains are always arranged alongside the build direction. The same microstructures are shown by the $0°_{XY}$-, $0°_{XZ}$-, 45°- and $90°_{Z}$-bars and they are consistent with those reported in [37,45,46].

As widely reported in the literature, the $\alpha' \rightarrow \alpha + \beta$ decomposition generates a microstructure where the primary, secondary and tertiary α-laths form a hierarchical structure such as the former $\alpha'$-martensite laths. Figures 5b and 5c illustrate the presence of this hierarchical structure where orange, green and light-blue dotted lines indicate the primary, secondary and tertiary α-laths, respectively. The EDS spectra of Table 3 confirm that the laths are the α-phase (spectrum A) and lighter zones are the β-phase (spectrum B) [47]. The former is characterized by a higher content of the α-stabilizer alloying element (Al), while the latter are richer in the β-stabilizing alloy elements (V and Fe) [19]. Huang et al. [32] affirmed that the microstructure shown in Figure 5b,d was strictly related, firstly, to the self-accommodation of the $\alpha'$-martensite and, secondly, to the Burgers relationships between the α and β phases.

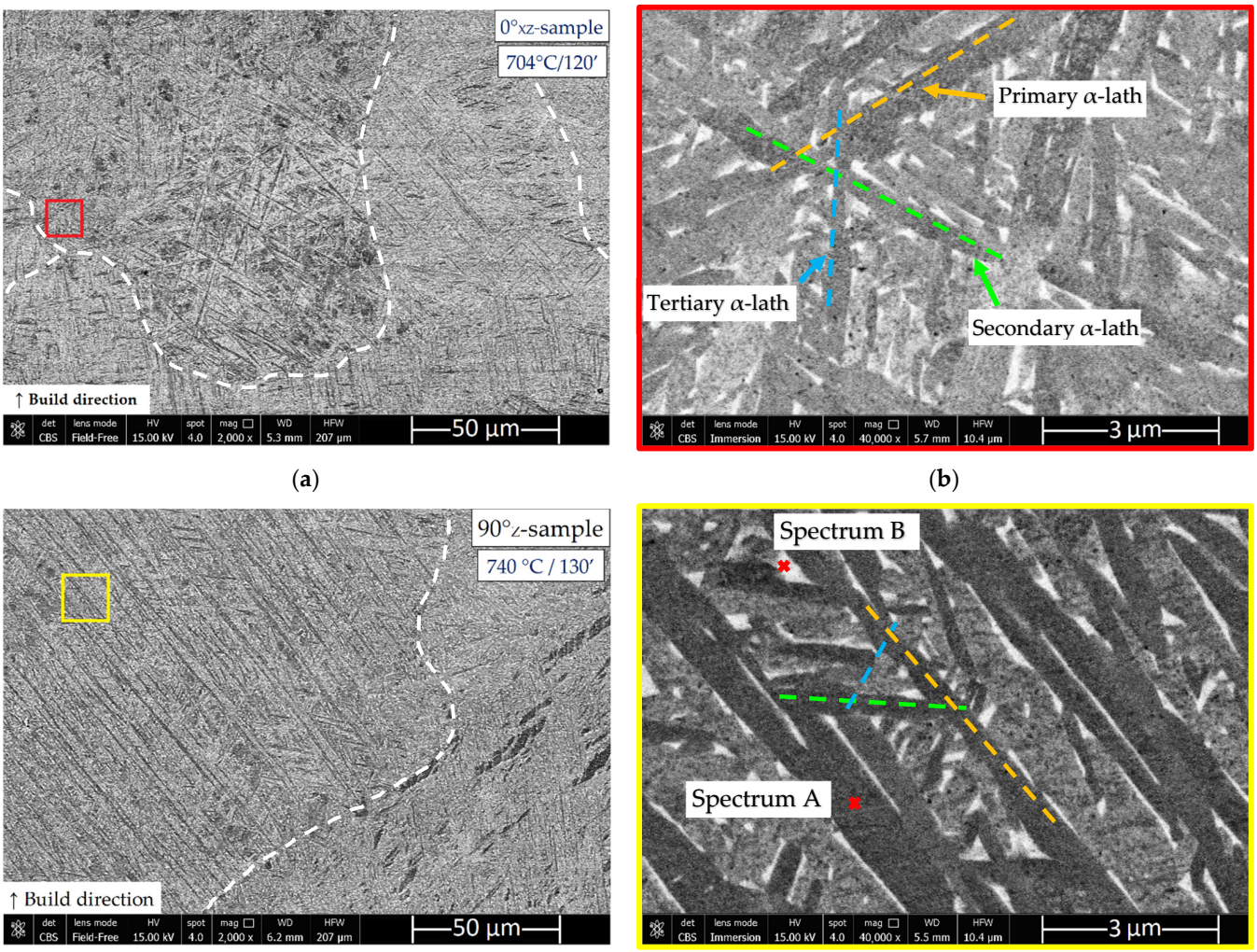


**Figure 5.** SEM micrographs of the $0°_{XY}$-sample (**a**,**b**) after 704 °C/120′ and $90°_{Z}$-sample (**c**,**d**) after 740 °C/130′. All images were acquired on the plane perpendicular to the build platform. Panel (**b**) illustrates the magnification (40 k×) of the red square area in panel (**a**) (2 k×), while panel (**d**) shows the magnification (40 k×) of the yellow square area in panel (**c**) (2 k×). Orange, green and light-blue dotted lines indicate primary, secondary and tertiary α-laths.

**Table 3.** Chemical composition (EDS) of spectra A and B in wt.%.

| Spectrum | Ti | Al | V | Fe | Phase |
|---|---|---|---|---|---|
| A | 91.6 | 7.2 | 1.2 | - | α |
| B | 89.9 | 2.0 | 7.9 | 0.2 | β |

In order to characterize the coarsening of the α-phase, its thickness was measured as a function of the heat-treatment conditions, and it increases from (540 ± 60) nm at 704 °C/120′ to (700 ± 10) nm at 740 °C/130′ due to the different temperatures and the furnace cooling from 740 to 520 °C in 90′. The same results were obtained in [29,48,49]. For example, Haar et al. [29] discussed the same phenomenon during the heat treatments in the low-SSTR (Solid Solution Temperature Region), i.e., at temperatures below 800 °C.

Increasing the heat-treatment temperature above the β-transus (T = 1050 °C), the columnar β-grains recrystallize into equiaxed grains, as shown in Figure 6a,b, where the microstructures of the $90°_{Z}$-sample (Figure 6a,c) and $90°_{Z}$-bar (Figure 6b,d) are shown. Figure 6c,d highlight the β-grain boundary formed by the $\alpha_{GB}$ (Grain Boundary) phase

due to $\beta \rightarrow \alpha_{GB}$ transformation during the cooling, and from which the $\alpha$-colonies and $\alpha$-laths nucleate and grow. Tensile samples are formed by $\alpha$-laths and small $\alpha$-colonies that form a typical basketweave structure within the equiaxed $\beta$-grains (Figure 6a,c). On the other hand, the bar is formed by the Widmanstätten microstructure (Figure 6b,d) where wider $\alpha$-colonies are arranged in a basketweave structure. In addition, Figure 6b shows a granular/globular $\alpha$-phase, as also shown in [50]. Ahmed et al. [51] suggested that different cooling rates induce these microstructural differences between the basketweave of $\alpha$-laths (<15 °C $s^{-1}$) and the classical "basketweave" Widmanstätten morphology (<1.5 °C $s^{-1}$). In the present work, the different cooling rates can be correlated to the different sample thicknesses between the tensile sample (6 mm) and the bar (10 mm) because both are simultaneously cooled with Argon gas for 1 h.

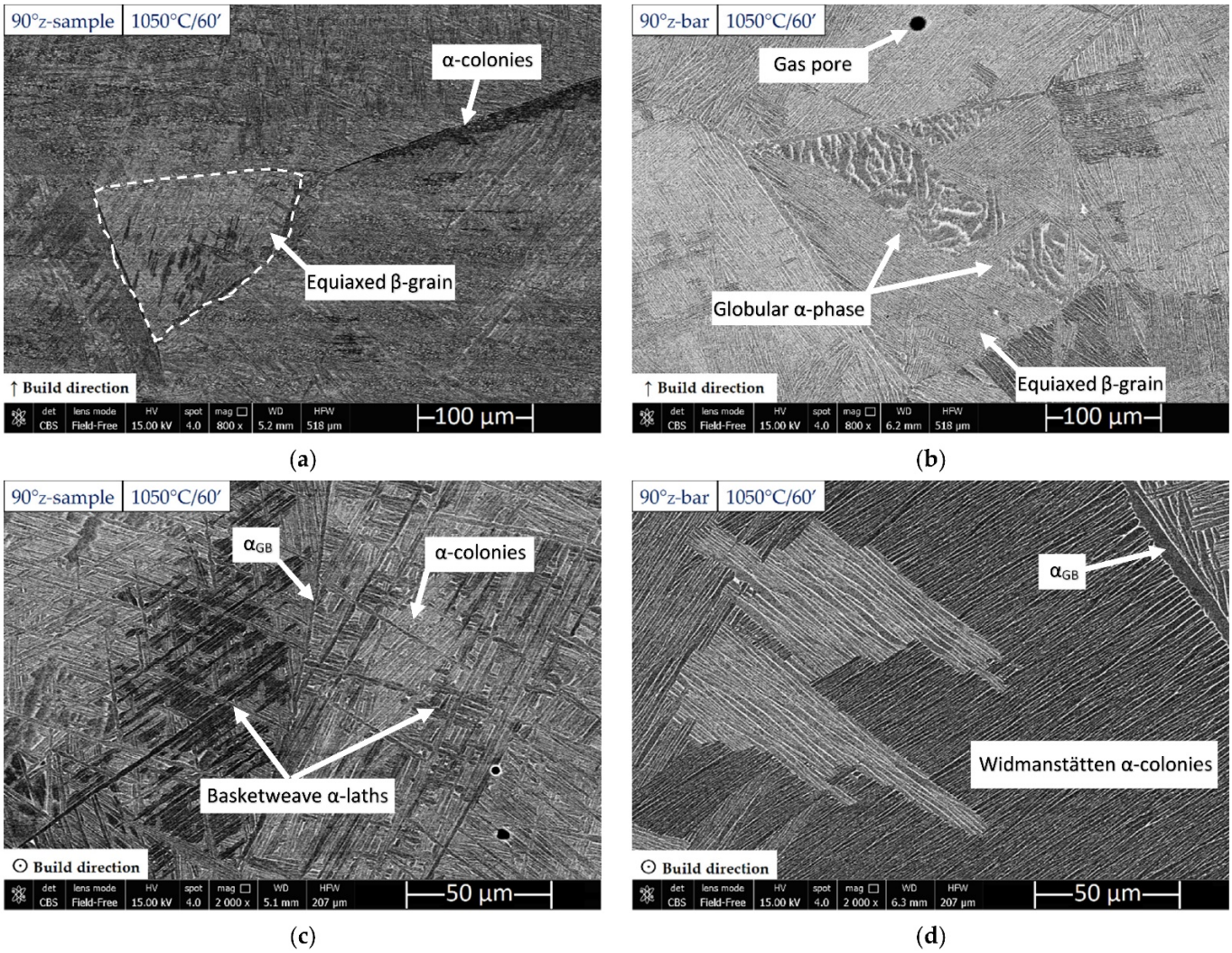


**Figure 6.** SEM micrographs of the 90°$_Z$-sample (**a**,**c**) and the 90°$_Z$-bar (**b**,**d**) acquired on the perpendicular (**a**,**b**) and parallel (**b**,**c**) planes to the build platform after 1050 °C/60′.

Heat treatment at 1050 °C/60′ also induces the formation of an $\alpha$-case surface layer with a thickness of 100 ÷ 150 µm and hardness of (400 ± 10) $HV_{0.1}$ in both the tensile sample (Figure 7a) and bar (Figure 7b). Similar results are shown in [49,52] for the cross-sections of the 45°-sample and 45°$_Z$-bar.

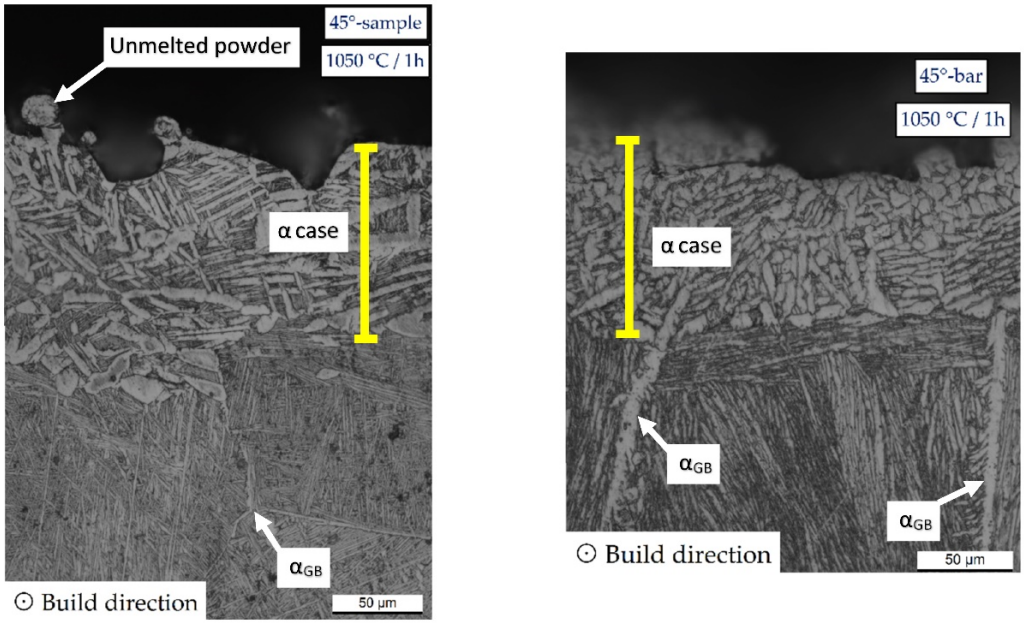


**Figure 7.** OM micrograph of the cross-section of the 45°-sample (**a**) and 45°-bar (**b**) after heat treatment at 1050 °C/60′.

Figure 8a shows the results of the XRD analysis performed on the cross-sections of the heat-treated $90°_Z$-samples after the 704 °C/120′, 740 °C/130′ and 1050 °C/60′ heat treatments. The different patterns show a reorientation and a possible recrystallization of the α-phase after the 1050 °C/60′, as previously reported and illustrated in Figures 5 and 6. Due to the exact overlap between the peaks of the α and α′ phases (as widely discussed in [12]), it is not possible to discern which of the two phases exists in each sample through XRD patterns alone. In this case, it is the microstructural observation in Figure 6 which confirms that the diffraction peaks of the samples heat-treated at 1050 °C belong to the α-phase rather than the α′-martensite. Instead, the peaks appearing in the patterns of the 704 °C/120′ and 740 °C/130′ samples can be ascribed to the α′/α-phases. The spectra also reveal peaks related to both the $\alpha_2$-$Ti_3Al$ and the $TiAl_3$ precipitates, which can be nucleated during the L-PBF process [12,24]. As a matter of fact, the heat treatments performed above 700 °C hardly cause precipitation phenomena in as-built Ti6Al4V-ELI samples because the precipitation temperatures of $\alpha_2$-$Ti_3Al$ and $TiAl_3$ are in the range of 500 ÷ 600 °C and 460 ÷ 515 °C, respectively [12,53]. In addition, the heat-treating temperature at 1050 °C did not induce the decomposition of these precipitates due to their higher decomposition temperature [12,54].

Figure 8b also highlights the effects induced by the sandblasting process on the surface of the heat-treated $90°_Z$-samples. Firstly, it exhibits the broadening of the diffraction peaks related to the α-phase due to the accumulation of plastic strain in the near-surface area. Secondly, the patterns related to the 1050 °C/60′ samples confirm that the sandblasting process removes the oxide formed during the heat treatment despite the inert-gas atmosphere.

Figure 9 illustrates the outer surface of the 45°-sample heat-treated at 704 °C/120′ before the sandblasting process. The $S_a$ value was (26 ± 2) µm. This illustration can be considered representative of the surfaces of all samples analyzed in the present manuscript. Indeed, the surface analyses performed on the $0°_{XY}$-, $0°_{XZ}$- and $90°_Z$-samples exhibits the same scanned layers on which different powder particles are partially melted, which are shown in Figure 9.

After the sandblasting process, the surface roughness of the 45°-sample heat-treated at 704 °C/120′ decreases to 12 ± 1 µm. In fact, Figure 10 shows a more uniform surface wherein the peak-to-valley distance is in the range of −80 ÷ 50 µm and not in the

−100 ÷ 120 µm one. In particular, the sandblasting process smoothed down the properties of the as built surface: the outer surface does not show the un-melted particles seen in Figure 9. Additionally, in this case, all SB samples are characterized by a $S_a$ in the range from 10 to 15 µm. At the same time, the $R_z$ values decrease from 170 ÷ 250 µm to 111 ÷ 160 µm in the no-SB and SB samples, respectively.

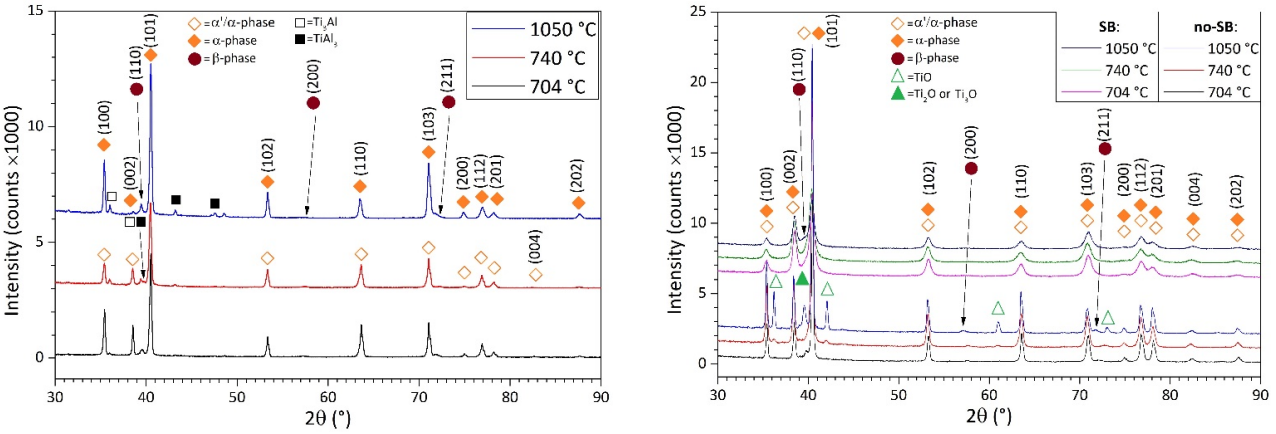


**Figure 8.** XRD patterns of heat-treated 90°$_Z$-samples at 704 °C/120′, 740 °C/130′ and 1050 °C/60′ performed on sand-blasted cross-sections (**a**), and on the external surface (**b**) before and after the sandblasting process.

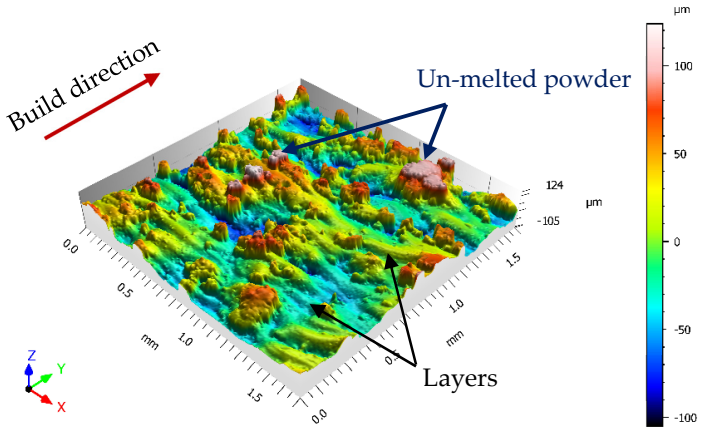


**Figure 9.** Topographical map of the 45°-sample heat-treated at 704 °C/120′ before the SB process.

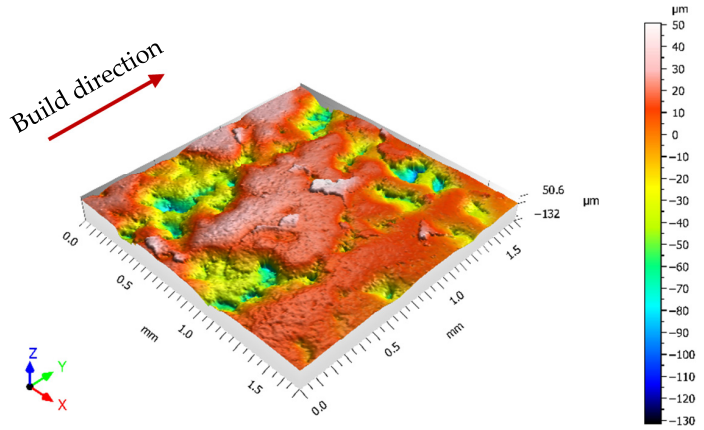


**Figure 10.** Topographical map of the 45°-sample heat-treated at 704 °C/120′ after the SB process.

### *3.2. Mechanical Properties*

The mechanical properties of no-SB and SB $0°_{XZ}$-, $0°_{XY}$-, 45°-, $90°_{Z}$-samples under all heat-treating conditions are shown in Figure 11. Focusing on the no-SB section of the graph, the samples heat-treated at 704 °C exhibit similar UTS, YS and elongation average values to the samples heat-treated at 740 °C (Table 4). On the other hand, the UTS and YS decrease up to 918 ± 7 MPa and 817 ± 6 MPa, respectively, after the treatment at 1050 °C/60′. The mechanical properties of the SB $0°_{XZ}$-, $0°_{XY}$-, 45°-, $90°_{Z}$-samples show the same trends, except for the elongation values at 1050 °C/60′. In this case, the average value decreases from 12.75 ± 1.01% in the no-SB case to 10.65 ± 0.21% in SB condition.

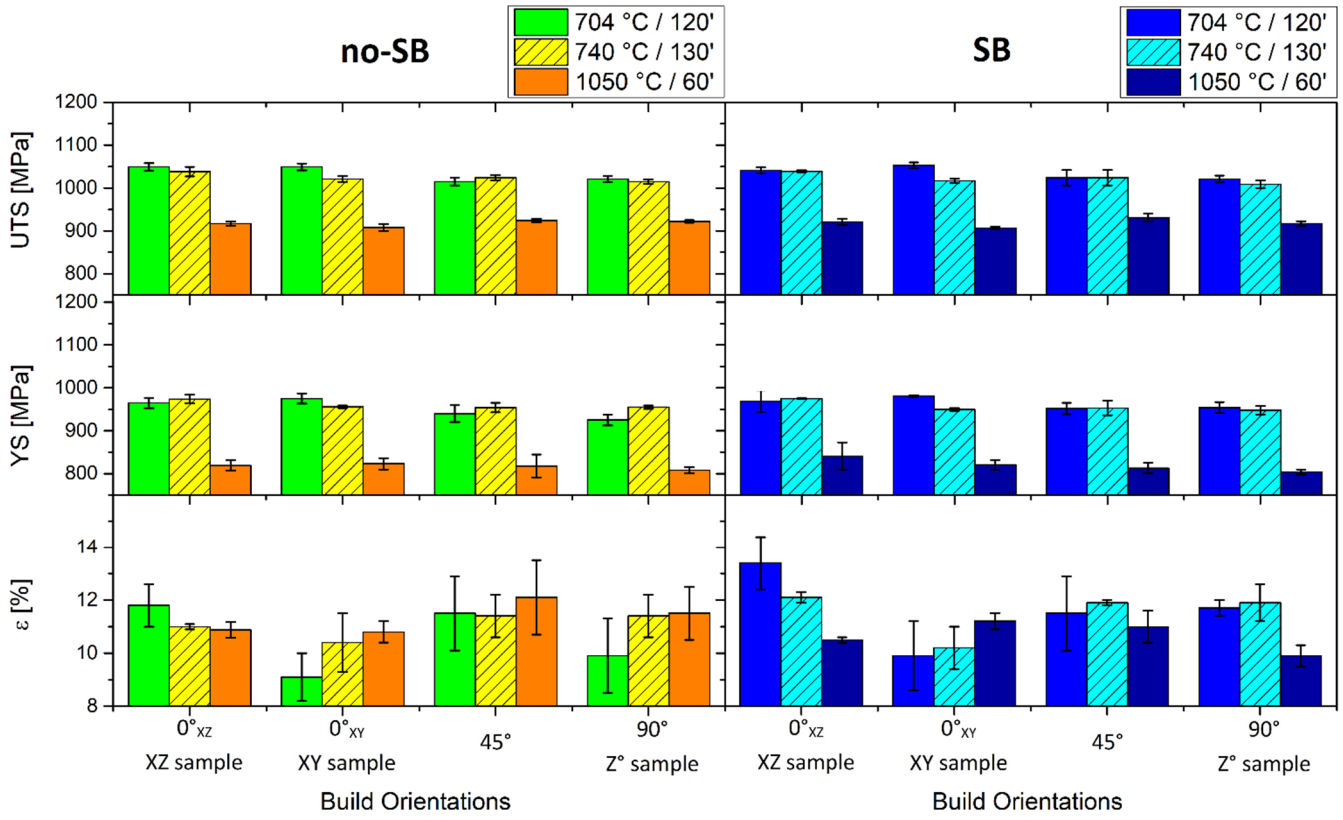


**Figure 11.** Mechanical properties of $0°_{XZ}$-, $0°_{XY}$-, 45°-, $90°_{Z}$-samples heat-treated at 704 °C/120′, 740 °C/130′ and 1050 °C/60′ in no-SB (**right section**) and SB (**left section**) conditions.

**Table 4.** Average values of the mechanical properties of no-SB and SB samples heat-treated at 704 °C/120′, 740 °C/130′ and 1050 °C/60′.

| Heat Treatments | No-SB | | | SB | | |
|---|---|---|---|---|---|---|
| | UTS [MPa] | YS [MPa] | ε [%] | UTS [MPa] | YS [MPa] | ε [%] |
| 704 °C/120′ | 1034 ± 18 | 948 ± 28 | 10.58 ± 0.69 | 1035 ± 5 | 964 ± 9 | 11.85 ± 0.5 |
| 740 °C/120′ | 1025 ± 10 | 960 ± 10 | 11.05 ± 0.49 | 1022 ± 7 | 957 ± 7 | 11.53 ± 0.35 |
| 1050 °C/60′ | 918 ± 7 | 818 ± 7 | 12.75 ± 1.01 | 919 ± 3 | 820 ± 11 | 10.65 ± 0.21 |

The effects induced by the sandblasting process are also analyzed on the cross-section of the $90°_{Z}$-sample through Vickers microhardness profiles (Figure 3b). Figure 12 correlates the $HV_{0.5}$ microhardness profiles of no-SB and SB samples for each heat-treatment temperature within the same graph. In addition, the orange, red and blue lines indicate the $HV_{0.5}$ average values of the 3rd–13th indentations, namely the $HV_{0.5}$ values obtained by excluding the possible effects induced by the sandblasting process. These values agree

with those reported in Table 5, which illustrates the $HV_{0.5}$ values of the heat-treated $0°_{XZ}$-, $0°_{XZ}$-, 45°-, $90°_{Z}$-bars and samples.

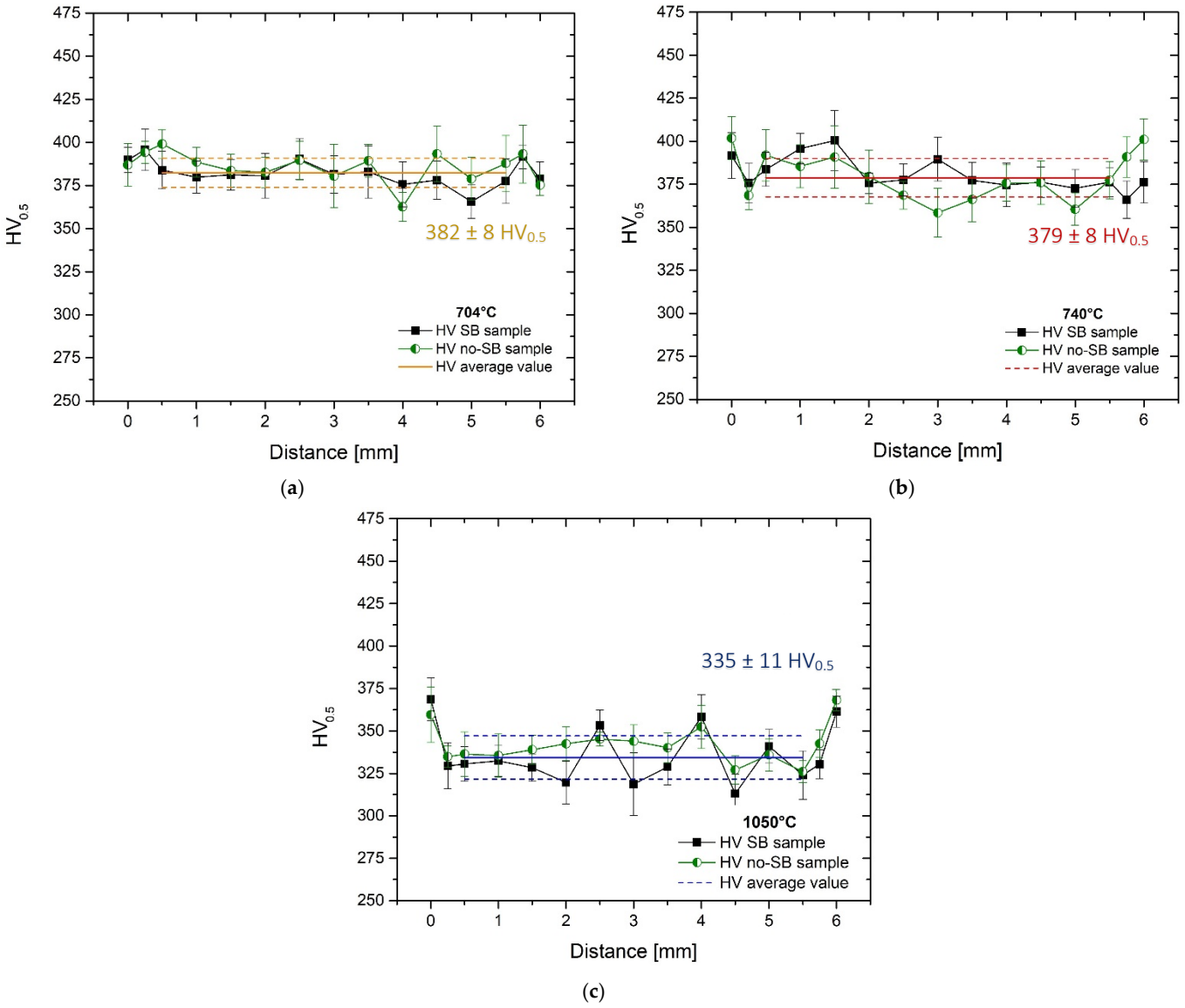


**Figure 12.** Vickers microhardness profile measured on the cross-section of $90°_{Z}$-samples heat-treated at: (**a**) 704 °C/120′, (**b**) 740 °C/130′ and (**c**) 1050 °C/60′. The orange, red and blue lines represent the $HV_{0.5}$ average values of the 3rd–13th indentations of the Vickers profiles, while the dotted lines show the associated error ranges.

**Table 5.** $HV_{0.5}$ measurements performed on heat-treated $0°_{XZ}$-, $0°_{XZ}$-, 45°-, $90°_{Z}$-bars (xz and xy planes) and samples (xz plane) at 704 °C/120′, 740 °C/130′ and 1050 °C/60′.

| Heat Treatments | $0°_{XZ}$- | | | $0°_{XY}$- | | | 45°- | | | $90°_{Z}$- | | |
|---|---|---|---|---|---|---|---|---|---|---|---|---|
| | Sample | Bar | | Sample | Bar | | Sample | Bar | | Sample | Bar | |
| | xz Plane | xy Plane | | xz Plane | xy Plane | | xz Plane | xy Plane | | xz Plane | xy Plane | |
| 704 °C/120′ | 387 ± 12 | 381 ± 15 | 374 ± 10 | 390 ± 10 | 379 ± 20 | 371 ± 19 | 381 ± 11 | 382 ± 10 | 368 ± 18 | 386 ± 6 | 381 ± 19 | 377 ± 15 |
| 740 °C/130′ | 375 ± 10 | 376 ± 17 | 361 ± 14 | 374 ± 6 | 370 ± 24 | 365 ± 21 | 372 ± 12 | 380 ± 12 | 370 ± 18 | 368 ± 10 | 374 ± 20 | 360 ± 18 |
| 1050 °C/60′ | 338 ± 5 | 341 ± 9 | 341 ± 8 | 336 ± 12 | 345 ± 8 | 343 ± 7 | 340 ± 9 | 339 ± 10 | 342 ± 8 | 339 ± 8 | 342 ± 5 | 348 ± 8 |

The hardness values measured on bars heat-treated at 704 °C/120′ and 740 °C/130′ agree with those obtained on the heat-treated tensile samples (Figure 12). As a matter of fact, the 704 °C/120′ and 740 °C/130′ bars show the same microstructure of the tensile

samples. Instead, considering the effects induced by the SHT at 1050 °C, the average $HV_{0.5}$ values of the bars are slightly higher than those obtained on the tensile sample due to the different microstructures (Figures 5 and 6). Figure 13 shows the $HV_{0.1}$ values of the different microstructures that form the 1050 °C/60′ heat-treated bars (Figure 13a–d) and tensile samples (Figure 13e,f). Increasing the thickness of α-laths that form the colonies (Figure 13a,b), the $HV_{0.1}$ value decreases from 398 $HV_{0.1}$ to 355 $HV_{0.1}$, while the lowest value was obtained by the globular α-phase. Focusing on tensile samples, 332 $HV_{0.1}$ was obtained for the basketweave α-laths in the center of the grain, while 392 $HV_{0.1}$ was obtained for the fine α-phase within the colony in the zone adjacent to the grain boundary. On the other hand, the $HV_{0.1}$ value of the $\alpha_{GB}$ decreases up to 335 $HV_{0.1}$ when considering the bar's microstructure (Figure 13d).

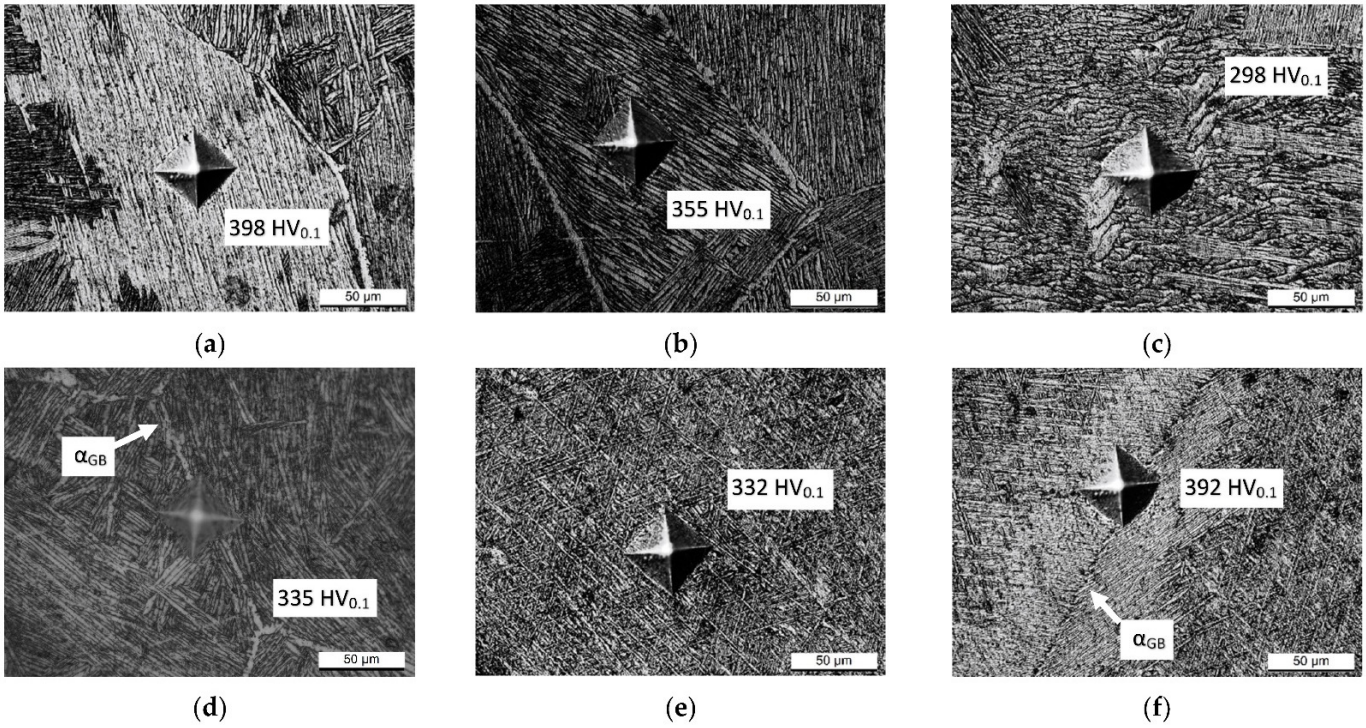


**Figure 13.** $HV_{0.1}$ indentations performed on different microstructures of the heat-treated 1050 °C/60′: (**a**–**d**) 90°$_z$-bar and (**e**,**f**) 90°$_z$-tensile sample.

## 4. Discussion

The as-built microstructure of the L-PBF Ti6Al4V-ELI samples (Figure 4) is characterized by columnar β-grains that grow parallel to the *z*-axis, or perpendicular to the xy plane, following the heat fluxes developed during the L-PBF process [55,56]. The β-grains nucleate from the build platform and grow across each of the deposited layers along the <100> as shown in Figure 4a [57]. As a matter of fact, the columns are arranged perpendicular to the molten pools. At the same time, they are contained within the laser scan tracks on the xy plane, as shown in Figure 4b. This configuration of the columnar β-grains characterized all samples regardless of the build orientations (Figures 4a and 5) [58]. The fully columnar structure is also confirmed by the relationships between the thermal gradient (G, (K/m)) and the solidification rate (R, (m/s)), which characterized the Ti6Al4V alloy during the L-PBF process [12]. In addition, the complex thermal history and the high cooling rate that characterized the L-PBF process induced the formation of α′-martensite, arranged in a hierarchical structure wherein the major axis of the primary α′ formed an angle of 45° with respect to the β-grain boundary [12,59–61]. Yang et al. [60] also affirmed that the α′-martensite forms an angle of 30 or 60° or 30 to 60° with respect to the build orientation. In the same context, Huang et al. [32] showed angles of 30, 60 and 90° between different

$\alpha'$-laths. This hierarchical structure of the $\alpha'$-martensite remains in the $\alpha$-laths developed after the heat treatments at 704 and 740 °C. Likewise, the columnar shape of the prior $\beta$-grains is also retained after those heat treatments. In particular, the $\alpha + \beta$ microstructure developed after the treatment below the $\beta$-transus presents primary, secondary and tertiary $\alpha$-phase arranged along the same orientations as the progenitor $\alpha'$-martensite laths. Haar et al. [29] confirmed the absence of quartic $\alpha$-laths due to the $\alpha'_{quartic}$-martensite $\rightarrow \beta$ decomposition. The XRD spectra, shown in Figure 8a, confirm a possible partial $\alpha' \rightarrow \alpha + \beta$ transformation due to the presence of peaks related to the $\beta$ phase, which are absent on the as-built XRD spectra [12]. TEM analysis discussed by Spigarelli et al. [62], which was performed on the same heat-treated samples, confirmed the presence of $\alpha'$martensite and, therefore, the incomplete $\alpha' \rightarrow \alpha + \beta$ transformation. Therefore, this validates the $\alpha'/\alpha$-phase labels shown on the XRD patters related to the samples heat-treated at 704 °C/120′ and at 740 °C/130′, respectively.

Because the $\alpha + \beta$ microstructure retains much of the features of the pristine $\alpha'$-martensite, the mechanical properties of both the heat-treated samples at 704 and 740 °C do not vary significantly (Figure 11 and Table 5). Therefore, the increase in the average thickness of the $\alpha$-laths from (540 ± 60) to (700 ± 10) nm, which can be caused by both the higher heat-treatment temperature and the first step of cooling up to 520 °C in 90′, does not influence the mechanical performance. Focusing on the error bars (Figure 14), which are obtained considering the tensile results of each build orientation (Figure 11), the samples heat-treated at 704 °C are characterized by a more pronounced anisotropy (ΔUTS = 4.75%, ΔYS = 7.40%) than those heat-treated at 740 °C (ΔUTS = 3.86%, ΔYS = 4.30%). These variations are calculated considering the maximum and minimum values of all build directions for each temperature. Vilaro et al. [46] reported ΔUTS = 4.40% and ΔYS = 6.74% after 730 °C/2 h with air cooling, while Simonelli et al. [63] did not detect any differences after the same heat treatment. As a matter of fact, the anisotropy depends significantly on the correlation between the load direction and both the lack-of-fusion (LOF) defects and the columnar $\beta$-grains [16,46,63,64]. The presence of $\alpha_2$ and/or $TiAl_3$ precipitates can be another possible contribution to the anisotropy, as will be later discussed. Therefore, future works related to the influence of LOF, grain boundaries and $\alpha$ phases may be necessary for the heat treatments analyzed in the present manuscript. The only influence of $\alpha$-phase coarsening is observable on the $HV_{0.5}$ microhardness values shown in Table 5.

During the SHT at 1050 °C for 60′, the recrystallization process of the columnar $\beta$-grains in equiaxed grains takes place (Figures 5 and 6), as also reported by [12,32,45,65]. The same results were obtained by Huang et al. [32] who suggested that the equiaxed grains form from the split of the progenitor columnar $\beta$-grains. Wu et al. [66], however, showed the recrystallization process already after 1000 °C/40′, followed by water quenching. Due to this microstructural change, together with the $\alpha$-laths in a basketweave structure (Figure 6), the UTS and YS values decrease (Figure 9) up to 918 ± 7 MPa and 817 ± 6 MPa, respectively; meanwhile, the elongation increases only up to 12.75 ± 1.01% due to both the $\alpha$-laths rather than $\alpha$-colonies in a basketweave structure (Figure 6a,c) and the possible detrimental effect of the $\alpha$-case [12,20,49,67]. The same tensile properties are confirmed by [19,32,68,69]. In this scenario, the mechanical properties of all heat-treated samples satisfy the minimum requirements dictated by the ASTM F3001 (UTS of 860 MPa, YS of 795 MPa and $\varepsilon$ of 8%). However, in relation to the samples heat-treated at 1050 °C/60′, the ASTM F3001-13a is not satisfied due to the presence of the $\alpha$-case layer. In fact, post-processing operations are required to remove the $\alpha$-case due to its worsening effects on fatigue life and ductility in aerospace components [2,49]. At the same time, the samples heat-treated at 704 and 740 °C, which are characterized by higher tensile properties than the solution heat-treated samples, also satisfy the F2924-14 standard specification (UTS of 895 MPa, YS of 825 MPa and $\varepsilon$ of 10%, [70]); this, however, is related to the Ti6Al4V alloy.

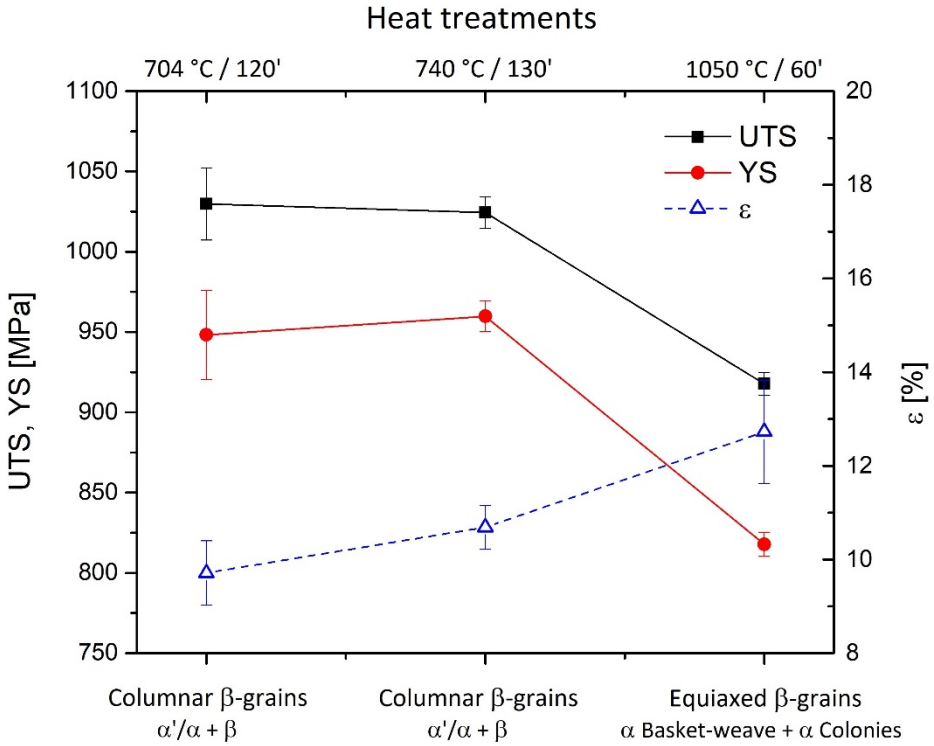


**Figure 14.** Average ultimate tensile strength, yield strength and elongation of the samples heat-treated at 704 °C/120′, 740 °C/130′ and 1050 °C/60′.

In relation to the cooling pathway, the Argon gas and the samples' thickness do not influence the microstructure of the samples heat-treated at 704 and 740 °C, as also reported in [29,33,68]. As a matter of fact, the cooling methods (water, air or gas, and furnace) have different effects in relation to the heat-treatment temperatures. In fact, the microstructure is not influenced by the cooling pathway if the cooling starts below ~800 °C [12,33,68]. By contrast, the $\beta \rightarrow \alpha'$-martensite transformation can take place when cooling starts from above 800 °C, as the sample is converted to β-phase and cooled at a high cooling rate. Ji et al. [71] affirmed that the critical temperature is around 870 °C. As previously reported, Kaschel et al. [29] demonstrated that the $\alpha'$-martensite starts to decompose at 400 °C and finishes at around 700 °C. Other authors, however, reported temperatures higher than 750 °C for $\alpha' \rightarrow \alpha + \beta$ decomposition [28,72,73]. Finally, the α-phase surely decomposes into β-phase following an exponential trend from ~800 °C to the β-transus temperature [29]. Focusing on the SHT treatment, the same cooling in Argon gas induces different microstructural morphologies (Figure 6) in relation to the sample thickness due to different cooling rates. Bars are characterized by α-colonies arranged in a basketweave (Widmanstätten) microstructure and globular α-phase (Figure 6c,d), while the tensile samples show α-laths in a basketweave structure within the equiaxed β-grain. At the same time, there are equiaxed grains formed by a mixture of α-laths at their center and α-colonies that nucleate and grow from the $\alpha_{GB}$ (Figure 6b). As previously reported, Ahmed et al. [51] confirmed that the Widmanstätten microstructure of α-laths and Widmanstätten microstructure of α-colonies form with cooling rates of 15 and 1.5 °C $s^{-1}$, respectively. Sieniawski et al. [74] showed that a rate of 9 °C $s^{-1}$ forms a mixture of α-colonies and α-laths. Generally, different cooling pathways from the β-region can induce a diffusionless $\beta \rightarrow \alpha'$-martensite transformation with a rate > 20 °C $s^{-1}$, or a $\beta \rightarrow \alpha + \beta$ diffusional transformation whereby the microstructure can assume different morphology with a rate < 20 °C $s^{-1}$ [12]. Gallaraga et al. [75] affirmed that the air cooling, which is characterized by a rate around 20 °C $s^{-1}$ from 1000 to 500 °C, can induce the nucleation of the $\alpha'$-martensite given that its Ms (Martensite start) temperature is $575 \leq T_{M_S} \leq 800$ °C [19].

Another important factor induced by the SHT at 1050 °C is the formation of the α-case layer as shown in Figure 7, both on tensile samples and bars. Seth et al. [49] affirmed that the α-case formation depends on the oxidizing capacity of the environment during heat-treating at high temperatures. As a matter of fact, the diffusion of oxygen atoms within the sample surface increases the β-transus temperature, as exhibited by the following equation:

$$T_{\beta-Tr} = 882 + 21.1[Al] - 9.5[Mo] + 4.2[Sn] - 6.9[Zr] - 11.8[V] - 12.1[Cr] - 15.4[Fe] + 23.3[Si] + 123.0[O] \quad (2)$$

where [element] represents the weight percentage of each element [76]. Kolachev et al. [77] proposed a similar linear relationship between the β-transus temperature and the chemical composition. Firstly, oxygen, as α-stabilizer alloying element [19], maintains a fraction of the α phase which does not undergo the $\alpha \rightarrow \beta$ transformation during the heat treatment. Secondly, it increases the $HV_{0.1}$ hardness, as shown in Figure 15, where the globular α-phase within the samples is characterized by 360 $HV_{0.1}$, while the α-case has a hardness of 403 $HV_{0.1}$.

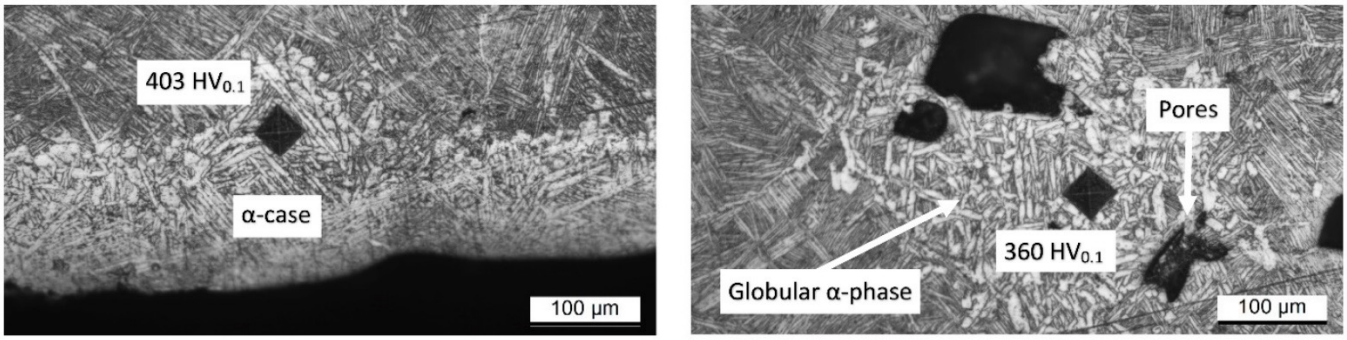


**Figure 15.** Representative $HV_{0.1}$ indentations performed on the α-case layer (**a**) and on the globular α-phases in the center of the bar (**b**).

The XRD analysis in Figure 8 confirms the presence of different titanium oxides on the sample surface and, therefore, the possible diffusion of oxygen atoms within the sample. At the same time, these patterns show the presence of $\alpha_2$-$Ti_3Al$ and $TiAl_3$ precipitates in different heat-treated samples. On the other hand, the XRD pattern performed on the cross-section of the $90°_Z$-sample (1) heat-treated at 740 °C (Figure 16) does not reveal any precipitate, despite it being manufactured and heat-treated in the same batch and direction as the $90°_Z$-sample (2). This can confirm that the high heat inputs developed during the L-PBF process generate different zones, persisting for an adequate time in the precipitation temperature range [27]. Therefore, a more detailed analysis on these precipitates will be performed in future works. Moreover, the differences between the precipitation phenomena between two equal heat-treated samples can explain the variability in terms of mechanical properties and $HV_{0.5}$ (Table 5) and, therefore, their anisotropy.

Comparing the mechanical properties of the no-SB and the SB samples, the sandblasting process performed after the different heat treatments does not induce any variation, except for the ductility values between the no-SB and SB samples heat-treated at 1050 °C/60′. The impact of the glass spheres on the sample surface induces plastic strain, as highlighted by the broadening of the α-peaks (Figure 8), and it can reduce the ductility. Future works on the effects of the sandblasting process on fracture mechanisms could be necessary. On the other hand, work-hardening was not detected by the Vickers hardness profiles on the cross-sections of all samples, as emphasized by the profiles in Figure 12. In particular, the average $HV_{0.5}$ values of the first and the last two points of each profile acquired on the 704 °C/120′ and 740 °C/130′ heat treatments (Figure 12a,b) do not significantly vary with respect to the hardness values measured at the center of the cross-section area; these are represented by the orange (Figure 12a) and red (Figure 12b) lines. In the 1050 °C/60′

samples, on the other hand, the $HV_{0.5}$ values next to the surface increase, but the same increase is seen for both the SB and no-SB samples (Figure 12c). This increase was, therefore, not a consequence of sandblasting; it was conferred by the presence of the α-case.

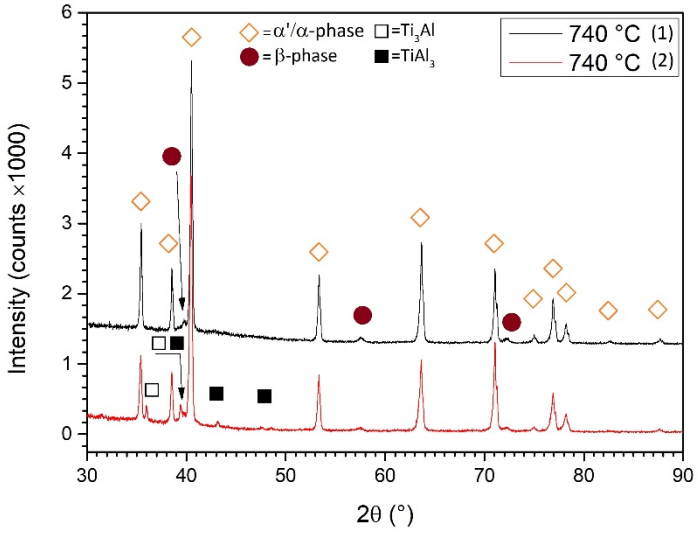


**Figure 16.** XRD patterns of two $90°_Z$-samples manufactured in the same batch and heat-treated at 740 °C/130′. The black XRD pattern (1) is correlated to the red pattern (2) that is the same shown in Figure 8a.

The reduction in the surface's roughness was another consequence of the sandblasting process. Considering that 3.2 μm is the recommended surface roughness for aerospace applications [78], all values obtained in the present work are unsatisfactory because the $R_a$ values decrease from 20 ÷ 28 μm to 10 ÷ 15 μm (Figures 9 and 10). On the other hand, the sandblasting post-process eliminates the presence of the un-melted particles on the surface and the oxides formed during the heat treatments (Figure 8).

## 5. Conclusions

The present paper aimed to evaluate the effects induced by different heat treatments (704 °C/120′, 740 °C/130′ and 1050 °C/60′), performed using an industrial furnace, on Ti6Al4V-ELI samples manufactured via Laser Powder-Bed Fusion in different build orientations. In addition, the effects of the sandblasting process were also analyzed. The main conclusions can be summarized as follows:

1. The microstructure of samples heat-treated at 704 and 740 °C is formed by columnar β-grains containing α′-martensite and α (primary, secondary and tertiary) + β phases. Some samples also showed $\alpha_2$-$Ti_3Al$ and $TiAl_3$ precipitates that are probably formed during the L-PBF process. These can cause the anisotropic behavior of the mechanical performance related to samples grown along the same direction.
2. The samples heat-treated at 704 °C show more anisotropic mechanical properties than the same tensile samples heat-treated at 740 °C. On the other hand, both satisfy ASTM F2924 and ASTM F3001 standard specifications. The increase in α-lath's thickness from 538 ± 66 to 704 ± 11 μm only influences the $HV_{0.1}$ microhardness measurements, but apparently has no effect on yield, ultimate tensile strength or elongation.
3. The microstructure of samples heat-treated at 1050 °C varies in relation to the sample's thickness. As a matter of fact, the tensile samples (6 mm) are formed by α-laths in a basketweave or Widmanstätten structure and small α-colonies within recrystallized equiaxed β-grains. Instead, bars (10 mm) are formed by wider α-colonies in a basketweave or Widmanstätten structure and globular α-phase within the same equiaxed β-grains. Moreover, in both cases, an α-case layer of about 100 ÷ 150 μm is formed on the surface.

4. The samples heat-treated at 1050 °C show mechanical properties that satisfy only the ASTM F3001 standard specification. Despite the decrease in UTS and YS by about 10% and 14%, respectively, the elongation values do not show a significant increase with respect to the samples heat-treated at 704 and 740 °C, probably due to the presence of the α-case layer.
5. The sandblasting process does not induce effects on the mechanical properties, but increases the plastic strain in the near-surface area. The obtained surface roughness of the sandblasted tensile sample (12 ÷ 16 µm) does not satisfy the requirements for aerospace applications.

**Author Contributions:** Conceptualization, E.C. and E.G.; methodology, E.C. and E.G.; software, E.G. and G.B.; validation, E.C.; formal analysis, E.G.; investigation, E.G. and G.B.; resources, E.C.; data curation, E.C. and E.G.; writing—original draft preparation, E.G.; writing—review and editing, E.C., E.G. and G.B.; supervision, E.C.; project administration, E.C. All authors have read and agreed to the published version of the manuscript.

**Funding:** This research received no external funding.

**Institutional Review Board Statement:** Not applicable.

**Informed Consent Statement:** Not applicable.

**Data Availability Statement:** All data are available within the manuscript.

**Acknowledgments:** The authors would like to thank BEAMIT (https://www.beam-it.eu/, accessed on 20 April 2022) for supplying the material.

**Conflicts of Interest:** The authors declare no conflict of interest.

## References

1. Froes, F.; Boyer, R.; Dutta, B. Introduction to aerospace materials requirements and the role of additive manufacturing. In *Additive Manufacturing for Aerospace Industry*, 1st ed.; Froes, F., Boyer, R., Eds.; Elsevier: Amsterdam, The Netherlands, 2017; pp. 1–6. [CrossRef]
2. Rugg, D.; Dixon, M.; Burrows, J. High-temperature application of titanium alloys in gas turbines. Material life cycle opportunities and threats—An industrial perspective. *Mater. High Temp.* **2016**, *233*, 536–541. [CrossRef]
3. Singh, P.; Pungotra, H.; Kalsi, N. On the characteristics of titanium alloys for the aircraft applications. *Mater. Today Proc.* **2017**, *4*, 8971–8982. [CrossRef]
4. Gurrapa, I. Characterization of titanium alloy Ti-6Al-4V for chemical, marine and industrial applications. *Mater. Charact.* **2003**, *51*, 131–139. [CrossRef]
5. Liu, Z.; He, B.; Lyu, T.; Zou, Y. A Review on Additive Manufacturing of Titanium Alloys for Aerospace Applications: Direct Energy Deposition and Beyond Ti-6Al-4V. *JOM* **2021**, *73*, 1804–1818. [CrossRef]
6. Inagaki, I.; Takechi, T.; Shirai, Y.; Ariyasu, N. Application and Features of Titanium for the Aerospace Industry. *Nippon Steel Sumimoto Met. Tech. Rep.* **2014**, *106*, 22–27.
7. Dutta, B.; Froes, F. The Additive Manufacturing (AM) of titanium alloy. *Met. Powder Rep.* **2017**, *72*, 96–106. [CrossRef]
8. Allen, J. *An Investigation into the Comparative Costs of Additive Manufacture vs. Machine Form Solid for Aero Engine Parts*; Rolls-Royce PLC Derby: Derbyshire, UK, 2006.
9. Ahmed, M.; Savvakin, D.; Ivasishin, O.; Pereloma, E. The effect of ageing on microstructure and mechanical properties of powder Ti-5Al-5Mo-5V-1Cr-1Fe alloy. *Mater. Sci. Eng. A* **2014**, *605*, 89–97. [CrossRef]
10. Sun, H.; Chu, X.; Liu, Z.; Gisele, A.; Zou, Y. Selective Laser Melting of Maraging Steels Using Recycled Powders: A Comprehensive Microstructural and Mechanical Investigation. *Metall. Mater. Trans. A* **2021**, *52*, 1714–1722. [CrossRef]
11. Watson, J.; Taminger, K. A decision-support model for selective additive manufacturing versus subtractive manufacturing based on energy consumption. *J. Clean. Prod.* **2018**, *176*, 1316–1322. [CrossRef] [PubMed]
12. Ghio, E.; Cerri, E. Additive Manufacturing of AlSi10Mg and Ti6Al4V lightweight alloys via Laser Powder Bed Fusion: A review of heat treatments effects. *Materials* **2022**, *15*, 2047. [CrossRef] [PubMed]
13. *ASTM 52900:2015(E)*; Standard Terminology for Additive Manufacturing-General Principles-Terminology. ASTM: West Conshohocken, PA, USA, 2000.
14. Gibbons, D.; Serfontein, J.-P.L.; van der Merwe, A.F. Mapping the path to certification of metal laser powder bed fusion for aerospace applications. *Rapid Prototyp. J.* **2021**, *27*, 355–361. [CrossRef]
15. Tang, M.; Pistorius, P.; Beuth, J.L. Prediction of a lack-of-fusion porosity for powder bed fusion. *Addit. Manuf.* **2017**, *14*, 39–48. [CrossRef]

16. Schwerz, C.; Nyborg, L. Linking In Situ Molten Pool Monitoring to Melt Size Distributions and Internal Flaws in Laser Powder Bed Fusion. *Metals* **2021**, *11*, 1856. [CrossRef]
17. He, Y.; Montgomery, C.; Beuth, J.; Webler, B. Melt pool geometry and microstructure of Ti6Al4V with B additions processed by selective laser melting additive manufacturing. *Mater. Des.* **2019**, *183*, 108126. [CrossRef]
18. Karayagiz, K.; Elwany, A.; Tapia, G.; Franco, B.; Johnson, L.; Ma, J.; Karaman, I.; Arróyane, R. Numerical and experimental analysis of heat distribution in the laser powder bed fusion of Ti-6Al-4V. *IISE Trans.* **2019**, *51*, 136–152. [CrossRef]
19. Boyer, R.; Welsch, G.; Colling, E.W. *Materials Properties: Handbook*; ASM International: Geauga County, OH, USA, 1994.
20. *ASTM F3001-14*; Standard Specification for Additive Manufacturing Titanium-6 Aluminium-4 Vanadium ELI (Extra Low Interstitial) with Powder Bed Fusion. ASTM: West Conshohocken, PA, USA, 2013.
21. Saboori, A.; Gallo, D.; Biamino, S.; Fino, P.; Lombardi, M. An Overview of Additive Manufacturing of Titanium Components by Direct Energy Deposition: Microstructure and Mechanical Properties. *Appl. Sci.* **2017**, *7*, 883. [CrossRef]
22. Bontha, S.; Klingbeil, N.; Kobrin, P.; Fraser, H. Thermal process maps for prediction solidification microstructure in laser fabrication of thin-wall structures. *J. Mater. Proc. Technol.* **2006**, *178*, 135–142. [CrossRef]
23. Ali, H.; Ma, L.; Ghadbeigi, H.; Mumtaz, K. In-situ residual stress reduction, martensitic decomposition and mechanical properties enhancement through high temperature powder bed pre-heating of selective laser melted Ti6Al4V. *Mater. Sci. Eng. A* **2017**, *695*, 211–220. [CrossRef]
24. Barriobero-Vila, P.; Gussone, J.; Haubrick, J.; Sandloebes, S.; Da Silva, J.; Cloentes, P.; Schell, N.; Raquerra, C. Inducing Stable α+β Microstructure During Selective Laser Melting of Ti-6Al-4V Using Intensified Intrinsic Heat Treatment. *Materials* **2017**, *10*, 268. [CrossRef]
25. Xu, W.; Brandt, M.; Sun, S.; Elambasseril, J.; Liu, Q.; Latham, K.; Xia, K.; Qian, M. Additive manufacturing of string and ductile Ti-6Al-4V by selective laser melting via in situ martensite decomposition. *Acta Mater.* **2015**, *85*, 74–84. [CrossRef]
26. Kaschel, F.; Vijayaraghavan, R.; Shmeliov, A.; McCarthy, E.; Canavan, M.; McNally, P.; Dowling, D.; Nicolosi, V.; Celikin, M. Mechanism of stress relaxation and phase transformation in additively manufactured Ti-6Al-4V via in-situ high temperature XRD and TEM analyses. *Acta Mater.* **2020**, *188*, 720–732. [CrossRef]
27. Xing, L.; Zhang, W.-J.; Zhao, C.-C.; Gao, W.-Q.; Shen, Z.-J.; Liu, W. Influence of Powder Bed Temperature on the Microstructure Mechanical Properties of Ti-6Al-4V Alloy Fabricated via Laser Powder Bed Fusion. *Materials* **2021**, *14*, 2278. [CrossRef]
28. Illarinov, A.; Stepanov, S.; Demakov, S. Effect of Thermomechanical Treatment Parameters on Structure, Phase Composition and Mechanical Properties of Ti-3Al-5Mo-4.5V Titanium Alloy. In Proceedings of the IOP Conference Series: Materials Science and Engineering, Chelyabinsk, Russia, 22–24 September 2020. [CrossRef]
29. Haar, G.; Becker, T. Selective Laser Melting Produced Ti-6Al-4V: Post-Process Heat Treatments to Achieve Superior Tensile Properties. *Materials* **2018**, *11*, 146. [CrossRef] [PubMed]
30. Sabban, R.; Bahl, S.; Chatterjee, K.; Suwas, S. Globularization using heat treatment in additively manufactured Ti-6Al-4V for high strength and toughness. *Acta Mater.* **2019**, *162*, 239–254. [CrossRef]
31. Muhammad, M.; Pegeus, J.; Shamsei, N.; Haghshenas, M. Effect of heat treatments on microstructure/small-scale properties of additive manufactured Ti-6Al-4V. *Int. J. Manuf. Technol.* **2019**, *103*, 4161–4172. [CrossRef]
32. Huang, Q.; Liu, X.; Yang, X.; Zhang, R.; Shen, Z.; Feng, Q. Specific heat treatment of selective laser melted Ti-6Al-4V for biomedical applications. *Front. Mater. Sci.* **2015**, *9*, 373–381. [CrossRef]
33. Lekoadi, P.; Tlotleng, M.; Annan, K.; Maledi, N.; Masina, B. Evaluation of Heat Treatment Parameters on Microstructure and Hardness Properties of High-Speed Selective Laser Melted Ti6Al4V. *Metals* **2021**, *11*, 255. [CrossRef]
34. Jaber, H.; Kónya, J.; Kulcsár, K.; Kovács, T. Effects of Annealing and Solution Treatments on the Microstructure and Mechanical Properties of Ti6Al4V Manufactured by Selective Laser Melted. *Materials* **2022**, *15*, 1978. [CrossRef]
35. Liu, S.; Shin, Y. Additive manufacturing of Ti6Al4V alloy: A review. *Mater. Des.* **2019**, *164*, 107552. [CrossRef]
36. Bai, H.; Deng, H.; Chen, L.; Liu, X.; Qin, X.; Zhang, D.; Liu, T.; Cui, X. Effect of Heat Treatment on the Microstructure and Mechanical Properties of Selective Laser-Melted Ti64 and Ti-5Al-5Mo-5V-1Cr-1Fe. *Metals* **2021**, *11*, 534. [CrossRef]
37. Tennant, R. Mechanical Surface in the Aerospace Industry. *Aircr. Eng. Aerosp. Technol.* **1992**, *64*, 4–14. [CrossRef]
38. Bower, K.; Murray, S.; Reinhart, A.; Nieto, A. Corrosion resistance of selective laser melted Ti-6Al-4V alloy in salt fog environment. *Res. Mater.* **2020**, *8*, 100122. [CrossRef]
39. Croll, S. Surface roughness profile and its effect on coating adhesion and corrosion protection: A review. *Prog. Org. Coat.* **2020**, *148*, 105847. [CrossRef]
40. Günter, J.; Krewerth, D.; Lippmann, T.; Leuders, S.; Tröster, T.; Weidne, A.; Biermann, H.; Niendorf, T. Fatigue life of additively manufactured Ti-6Al-4V in the very high cycle fatigue regime. *Int. J. Fatigue* **2017**, *94*, 236–245. [CrossRef]
41. Zhang, H.; Dong, D.; Su, S.; Chen, A. Experimental study of effect of post processing on fracture toughness and fatigue crack growth performance of selective laser melting Ti-6Al-4V. *Chin. J. Aeronaut.* **2019**, *32*, 2383–2393. [CrossRef]
42. Möller, H.; Curle, U. Fatigue and Fracture Toughness of Ti-6Al-4V Titanium Alloy Manufactured by Selective Laser Melting. *Adv. Mater. Res.* **2014**, *1019*, 248–253. [CrossRef]
43. Gallaraga, H.; Lados, D.; Dehoff, R.; Kirka, M.; Nandwana, P. Effect of the microstructure and porosity of Ti-6Al-4V ELI alloy fabricated by electron beam melting (EBM). *Addit. Manuf.* **2016**, *10*, 45–57. [CrossRef]
44. Tiley, J.; Searles, T.; Lee, E.; Kar, S.; Banerjee, R.; Russ, J.; Fraser, H. Quantification of microstructural features in α/β titanium alloys. *Mater. Sci. Eng. A* **2004**, *372*, 191–198. [CrossRef]

45. Eshawish, N.; Malinov, S.; Sha, W.; Wallas, P. Microstructure and Mechanical Properties of Ti-6Al-4V Manufactured by Selective Laser Melting after Stress Relieving, Hot Isostatic Pressing Treatment, and Post-Heat Treatment. *J. Mater. Eng. Perform.* **2021**, *30*, 5290–5296. [CrossRef]
46. Vilaro, T.; Colin, C.; Bartout, J. As-fabricated and Heat-treated microstructures of the Ti-6Al-4V alloy processed by Selective Laser Melting. *Mater. Trans. A* **2011**, *42*, 3190–3199. [CrossRef]
47. Qiao, Y.; Xu, D.; Wnag, S.; Ma, Y.; Chen, J.; Wnag, Y.; Zhou, H. Corrosion and Tensile Behaviors of Ti-6Al-2V-1Mo-1Fe and Ti-6Al-4V Titanium Alloys. *Metals* **2019**, *9*, 1213. [CrossRef]
48. Cao, S.; Chen, Z.; Lim, C.; Yang, K.; Jia, Q.; Jarvis, T.; Tomus, D.; Wu, X. Defect, Microstructure, and Mechanical Property of Ti-6Al-4V Alloy Fabricated by High-Power Selective Laser Melting. *JOM* **2017**, *96*, 2684–2692. [CrossRef]
49. Seth, P.; Jha, J.; Alankar, A.; Mishra, S. Alpha-case Formation in Ti-6Al-4V in a Different Oxidizing Environment and Its Effect on Tensile and Fatigue Crack Growth Behavior. *Oxid. Met.* **2022**, *97*, 77–95. [CrossRef]
50. Nie, B.; Zhao, Z.; Chen, D.; Liu, S.; Lu, M.; Zhang, J.; Liang, F. Effect of Basketweave Microstructure on Very High Cycle Fatigue Behavior of TC21 Titanium Alloy. *Metals* **2018**, *8*, 401. [CrossRef]
51. Ahmed, T.; Rack, H. Phase transformations during cooling in α+β titanium alloys. *Mater. Sci. Eng. A* **1998**, *243*, 206–211. [CrossRef]
52. Chicos, L.-A.; Zaharia, S.; Lancea, C.; Pop, M.; Cañadas, I.; Rodrìguez, J.; Galindo, J. Concentrated solar energy used for heat treatment of Ti6Al4V alloy manufactured by selective laser melting. *Solar Energy* **2018**, *173*, 76–88. [CrossRef]
53. Zhao, X.-A.; So, F.; Nicolet, N.-A. TiAl3 formation by furnace annealing of Ti/Al bilayers and the effects of impurities. *J. Appl. Phys.* **1988**, *63*, 2600–2607. [CrossRef]
54. Ohnuma, I.; Fujita, Y.; Mitsui, H.; Ishikawa, K.; Kainuma, R.; Ishida, K. Phase equilibria in the Ti-Al binary system. *Acta Mater.* **2000**, *48*, 3113–3123. [CrossRef]
55. Antonisamy, A.; Meyer, J.; Prangnell, P. Effect of build geometry on the β-grains structure and texture in additive manufacture of Ti-6Al-4V by selective electrons beam melting. *Mater. Charact.* **2015**, *632*, 505–513. [CrossRef]
56. Wang, T.; Zhou, Y.; Zhang, S.; Tang, H.; Wang, H. Grain morphology evolution behaviour of titanium alloy components during laser melting deposition additive manufacturing. *J. Alloys Compd.* **2021**, *13*, 1159–1168. [CrossRef]
57. Qi, M.; Huang, S.; Ma, Y.; Youssef, S.; Zhang, R.; Qiu, J.; Lei, J.; Yang, R. Columnar to equiaxed transition during β heat treatment in a near β alloy by laser additive manufacture. *J. Mater. Res. Technol.* **2021**, *13*, 1159–1168. [CrossRef]
58. Sui, Q.; Li, P.; Wnak, K.; Yin, X.; Liu, L.; Zhang, Y.; Zhang, Q.; Wang, S.; Wang, L. Effect of Build Orientation on the Corrosion Behavior and Mechanical Properties of Selective Laser Melted Ti-6Al-4V. *Metals* **2019**, *9*, 976. [CrossRef]
59. Salsi, E.; Chiumenti, M.; Cervera, M. Modeling of Microstructure Evolution of Ti6Al4V for Additive Manufacturing. *Metals* **2018**, *8*, 633. [CrossRef]
60. Yang, J.; Yu, H.; Yin, J.; Gao, M.; Wang, Z.; Zeng, X. Formation and control of martensite in Ti-6Al-4V alloy processed by selective laser melting. *Mater. Des.* **2016**, *108*, 308–318. [CrossRef]
61. Pantawane, M.; Ho, Y.; Joshi, S.; Dahotre, N. Computational Assessment of Thermokinetics and Associated Microstructural Evolution in Laser Powder Bed Fusion Manufacturing of Ti6Al4V Alloy. *Sci. Rep.* **2020**, *10*, 7579. [CrossRef] [PubMed]
62. Spigarelli, S.; Paoletti, C.; Cabibbo, M.; Cerri, E.; Santecchia, E. On the creep performance of the Ti-6Al-4V alloy processed by additive manufacturing. *Addit. Manuf.* **2022**, *49*, 102520. [CrossRef]
63. Simonelli, M.; Tse, Y.Y.; Tuck, C. Effect of the building orientation on the mechanical properties and fracture modes of SLM Ti-6Al-4V. *Mater. Sci. Eng. A* **2014**, *616*, 1–11. [CrossRef]
64. Hartunian, P.; Eshraghi, M. Effect of Build Orientation on the Microstructure and Mechanical Properties of Selective Laser-Melted Ti-6Al-4V Alloy. *J. Manuf. Mater. Process.* **2018**, *2*, 69. [CrossRef]
65. Bartsch, K.; Hergoz, D.; Bossen, B.; Emmelmann, C. Material modelling of Ti-6Al-4V processed by laser powder bed fusion for application for application in macro-scale process simulation. *Mater. Sci. Eng. A* **2021**, *814*, 141237. [CrossRef]
66. Wu, S.; Lu, Y.; Gan, Y.; Huang, T.; Zhao, C.; Lin, J.; Guo, S.; Lin, J. Microstructural evolution and microhardness of selective-laser-melted Ti-6Al-4V alloy after post heat treatments. *J. Alloys Compd.* **2016**, *672*, 643–652. [CrossRef]
67. Jha, J.S.; Toppo, S.P.; Singh, R.; Tewari, A.; Mishra, S.K. Deformation behavior of Ti-6Al-4V microstructures under uniaxial loading: Equiaxed Vs. transformed-β microstructures. *Mater. Charact.* **2021**, *171*, 110780. [CrossRef]
68. Vrancken, B.; Thijs, L.; Kruth, J.; Humbeeck, J. Heat treatments of Ti6Al4V produced by Selective Laser Melting: Microstructure and mechanical properties. *J. Alloy. Compd.* **2012**, *541*, 177–185. [CrossRef]
69. Leuders, S.; Lieneke, T.; Lammers, S.; Tröster, T.; Niendorf, T. On the fatigue properties of metals manufactured by selective laser melting—The role of ductility. *J. Mater. Res.* **2014**, *29*, 1911–1919. [CrossRef]
70. *ASTM F2924-12*; Standard Specification for Additive Manufacturing Titanium-6 Aluminium-4 Vanadium with Powder Bed Fusion. ASTM: West Conshohooken, PA, USA, 2013.
71. Ji, Y.; Heo, T.; Zhang, F.; Chen, L. Theoretical Assessment on the Phase Transformation Kinetic Pathways of Multi-Component Alloys: Application to Ti-6Al-4V. *J. Phase Equilibria Diffus.* **2016**, *54*, 149–158. [CrossRef]
72. Sallica-Leva, E.; Caram, R.; Jardini, A.; Fagagnolo, J. Ductility improvement due to martensite α' decomposition in porous Ti-6Al-4V parts produced by selective laser melting for orthopedic implants. *J. Mech. Behav. Biomed. Mater.* **2016**, *54*, 149–158. [CrossRef] [PubMed]

73. Cao, S.; Chu, R.; Zhou, X.; Yang, K.; Jia, Q.; Lim, C.S.; Huang, A.; Wu, X. Role of martensite decomposition in tensile properties of selective laser melted Ti-6Al-4V. *J. Alloy. Compd.* **2018**, *744*, 357–363. [CrossRef]
74. Sieniawski, J.; Ziaja, W.; Kubiac, K.; Motyka, M. Microstructure and Mechanical Properties of High-Strength Two-Phase Titanium Alloys. In *Titanium Alloys—Advances in Properties Control*; Sieniawski, J., Ziaja, W., Eds.; IntechOpen: London, UK, 2013. [CrossRef]
75. Gallaraga, H.; Warren, R.; Lados, D.; Dehoff, R.; Kirka, M.; Nandwana, P. Effects of heat treatments on microstructure and properties od Ti-6Al-4V ELI alloys fabricated by electron beam melting (EBM). *Mater. Sci. Eng. A* **2017**, *685*, 417–428. [CrossRef]
76. Guo, Z.; Malinov, S.; Sha, W. Modelling beta transus temperature of titanium alloys using artificial neural network. *Comput. Mater. Sci.* **2005**, *32*, 1–12. [CrossRef]
77. Kolachev, B.; Egorova, Y.; Belova, S. Relation between the temperature of the $\alpha + \beta \rightarrow \beta$ transformation of commercial titanium alloys and their chemical composition. *Met. Sci. Heat Treat.* **2008**, *50*, 367–372. [CrossRef]
78. Bagehorn, S.; Wehr, J.; Maier, H. Application of mechanical surface finishing processes for roughness reduction and fatigue improvement of additvely manufactured Ti-6Al-4V parts. *Int. J. Fatigue* **2017**, *102*, 135–142. [CrossRef]